

Article

Solar Flare Effects Observed over Mexico during 30–31 March 2022

Maria A. Sergeeva ^{1,2,*}, Olga A. Maltseva ³, Artem M. Vesnin ⁴, Donat V. Blagoveshchensky ⁵, Victor J. Gatica-Acevedo ¹, J. Americo Gonzalez-Esparza ¹ , Aleksandr G. Chernov ⁶, Isaac D. Orrala-Legorreta ^{1,7}, Angela Melgarejo-Morales ¹, Luis Xavier Gonzalez ^{1,2}, Mario Rodriguez-Martinez ⁸ , Ernesto Aguilar-Rodriguez ¹, Ernesto Andrade-Mascote ¹ and Pablo Villanueva ¹

¹ SCiESMEX, LANCE, Instituto de Geofisica, Unidad Michoacan, Universidad Nacional Autonoma de Mexico, Morelia C.P. 58089, Michoacan, Mexico

² CONACYT, Instituto de Geofisica, Unidad Michoacan, Universidad Nacional Autonoma de Mexico, Morelia C.P. 58089, Michoacan, Mexico

³ Institute for Physics, Southern Federal University, 344090 Rostov-on-Don, Russia

⁴ Institute of Solar-Terrestrial Physics, Siberian Branch of Russian Academy of Sciences, 664033 Irkutsk, Russia

⁵ Institute of Radio Engineering and Information and Communications Technologies, Saint-Petersburg State University of Aerospace Instrumentation, 190000 Saint-Petersburg, Russia

⁶ Sitcomm LLC, 424031 Yoshkar-Ola, Russia

⁷ Facultad de Ciencias, Universidad Nacional Autonoma de Mexico, Coyoacán C.P. 04510, Mexico City, Mexico

⁸ Escuela Nacional de Estudios Superiores, Unidad Morelia, Universidad Nacional Autonoma de Mexico, Morelia C.P. 58190, Michoacan, Mexico

* Correspondence: maria.a.sergeeva@gmail.com



Citation: Sergeeva, M.A.; Maltseva, O.A.; Vesnin, A.M.; Blagoveshchensky, D.V.; Gatica-Acevedo, V.J.; Gonzalez-Esparza, J.A.; Chernov, A.G.; Orrala-Legorreta, I.D.; Melgarejo-Morales, A.; Gonzalez, L.X.; et al. Solar Flare Effects Observed over Mexico during 30–31 March 2022. *Remote Sens.* **2023**, *15*, 397. <https://doi.org/10.3390/rs15020397>

Academic Editor: Fabio Giannattasio

Received: 28 November 2022

Revised: 27 December 2022

Accepted: 28 December 2022

Published: 9 January 2023



Copyright: © 2023 by the authors. Licensee MDPI, Basel, Switzerland. This article is an open access article distributed under the terms and conditions of the Creative Commons Attribution (CC BY) license (<https://creativecommons.org/licenses/by/4.0/>).

Abstract: Manifestations of two solar flares of March 2022 were studied over Mexico. The flare effects in the lower ionosphere had a ~3 min delay from the X1.3-flare onset and ~5 min from the M9.6-flare onset. The maximal impact on the HF signal amplitude was ~(14–15) min after the onset of both flares. The X1.3-flare provoked the shortwave fadeout during ~6 min. The effects in the lower ionosphere lasted longer than the flares and the effects at the F2 region and higher altitudes only during the flares. The interpretation of results showed the following. (1) Based on the absorption level estimated with minimum frequency and signal amplitude on ionograms, the major role of X-ray radiation in the electron concentration increase in the lower ionosphere was confirmed. At the same time, the EUV radiation impact on the lower ionosphere cannot be totally discarded. The lower ionosphere recovery began before and lasted after the X1.3-flare end, being more rapid at Eglin than in Mexico. During M9.6-flare, the responses at the two observation points were rather synchronized due to the more similar illumination conditions at the two meridians. (2) According to the dI variations characterizing the F2 region and higher, the M9.6-flare provoked medium-scale and the X1.3-flare provoked both medium- and small-scale ionospheric irregularities. The response duration corresponded to the dI series filtered with (10–20) min windows. The dI curve during the flares was characterized by the H-form and depended more on the active region position and the flare class than on the solar zenith angle. The available data do not allow us to unambiguously identify the reason for the negative dI: the applied filtering procedure or the physical effect. (3) During both flares, the major EUV impact on the lower ionosphere was by the flux at 133.5 nm and on the F2 region and higher altitudes at 25.6 nm. In addition, during the M9.6-flare, EUV 28.4, 30.4 and 121.6 nm spectral bands also played an important role in the F2 response. During the X1.3-flare, the EUV 25.6 nm flux and X-ray flux impacts on the F2 region were of the same level. The weakest impact was caused by the emission in the EUV 28.4 nm spectral band on the absorption in the lower ionosphere during both flares and on the electron density in the F2 region and higher during the X1.3-flare.

Keywords: solar flare; ionosphere; ionospheric sounding; ionosonde; GNSS; slant TEC; Mexico

1. Introduction

Ionospheric disturbances determine ionospheric parameter deviations from their quiet diurnal values with characteristic time scales from some minutes to several days. The ionosphere can be perturbed by different factors. Sometimes, the effects of different sources superpose.

Sudden Ionospheric Disturbances (SID) are the ionization increases of the dayside ionosphere caused by the bursts of ultraviolet and X-ray radiation from the Sun during solar flares. Sharp increases in solar X-rays ionizing radiation result in an increase of the ionization velocity and eventually in the corresponding electron concentration increases in the D and lower E regions of the ionosphere. SIDs in the upper E and F regions that are mostly ionized by ultraviolet radiation are usually less pronounced and of less duration [1]. Significant increases of radiation affect radio propagation conditions [2]. Each particular flare is a unique event, and the ionospheric response to it can vary. In the worst case, the total absorption of the energy of radio waves propagating by reflection in the ionosphere is observed. In general, the electron concentration increase caused by the intense flares is maximal within altitudes of 60–85 km. It can also reach 50–200% in the ionospheric E region and 10–30% in the F region [1,3].

In this work, we estimate the impacts of two intense flares (X1.3 and M9.6) that occurred on 30 and 31 March 2022 on the topside and the lower ionosphere over the Mexican region. Since the flares occurred close to the Mexican noon, its territory was most affected by the flares.

Data of different instruments may be used to estimate the flare impact on the ionosphere in general and the absorption level in particular, for example radars, e.g., [4,5], riometers (mostly at high-latitudes) e.g., [6], ionospheric sounding (ionosonde) data e.g., [7,8], satellite-to-ground radio methods [9,10], VLF signal data (including signal amplitudes) e.g., [11,12] and others.

The attenuation of HF radio waves is due to absorption in the lower ionosphere [2,3,13]. The fadeout events occur more often at high-latitudes [14]. Our focus is on the low- to mid-latitudes of the North American sector.

Intense solar flares can also perturb the ionosphere at higher altitudes, namely at the F2-layer heights and in the topside ionosphere [15–19] and references therein. One of the approaches to study the effects at these heights is the use of slant and/or vertical Total Telectron Content (TEC) data (e.g., [19]). Habarulema et al. [20], citing the articles of 2021, pointed out that the flare effects can extend to geospace, which emphasizes the importance of TEC use for analysis. Similar to Habarulema et al. [20], we had the opportunity to involve both TEC and ionospheric sounding data. The peculiarity of the present study is the high temporal resolution of the ionosonde data (ionograms taken each 2 min) and the GNSS-derived filtered slant TEC (sTEC) data (time series resolution of 30 s).

There are many statistical and case studies on solar flare's influence on the ionosphere (we only mention some of them not to overload the text with numerous references that the reader can find in the review papers). Nonetheless, to date, the interest in studying flare effects, especially within the ionospheric regional context, has not faded. This is partially explained by the variability of the ionospheric responses to this type of Space Weather disturbance. As shown by Barta et al. and Habarulema et al. [7,20], the flare effects have been studied most frequently for the European and African regions. This study is focused on the low latitudes of the North American sector. Recently, Le et al. [21] revealed an interesting feature for this region. According to these authors, some flares resulted in TEC enhancements being the highest, not near the subsolar point, but rather far away from it. They found that the anomaly distributions of TEC deviations were observed mainly in the North American region during the flares that occurred in September–November. Though our study is focused on spring flares, such results indicate the overall importance of the studies for this region. During equinoxes, the ionospheric response to flares is more pronounced than during solstice periods because of the seasonal variation of neutral

density [22]. This is our case, as the considered flares occurred 10 days after the spring equinox in 2022.

This paper is organized as follows. Section 2 provides a description of the two flares considered. Section 3 introduces the data used for the study. Section 4.1 discusses the flare effects on the lower ionosphere (D and lower E regions) revealed with the ionospheric sounding data. Section 4.2 presents the results of the flare effect detection at the higher ionospheric heights (from the F2 region to the topside ionosphere). Final remarks are given in Conclusions.

2. Description of the Considered Flares

Two intense solar flares occurred near the midday local time of the American sector on 30 and 31 March 2022. The flare parameters are given in Table 1. There are similarities and differences in the observation conditions of the considered events. Both were caused by the same active region (AR) on the solar disk (Figure 1), which was disappearing due to solar rotation (Figure 2). In addition to the close local time of occurrence (LT), both flares had comparable durations and occurred under undisturbed geomagnetic conditions. However, though the two events occurred on two consecutive days, meaning the same total daylight duration and seasonal conditions, there was a difference in the solar activity represented by the F10.7-index and some difference in the geomagnetic conditions. Note that no magnetic storm occurred on the flare days or before. Notwithstanding the F10.7 and Dst variations, it was possible to observe exactly the flare effects. The intensity of the flares was different.

Table 1. Parameters of the considered flares and conditions of their observation.

Date	Flare Onset, UT	Flare Max, UT	Flare End, UT	Duration (Phases), Min	LT = ~(UT-5)	X-Class	AR (Coordinates)	F10.7, s.f.u (at 20 UT)	Dst * (Daily max/min), nT
30 March 2022 DOY = 089	17:21	17:37	17:46	25 (16 + 9)	12:21 LT	X1.3	2975 (N13W31)	151.3	10/-9
31 March 2022 DOY = 090	18:17	18:35	18:45	28 (18 + 10)	13:17 LT	M9.6	2975 (N12W47)	239.5	22/-18

* Dst values are given only to characterize the overall background conditions.

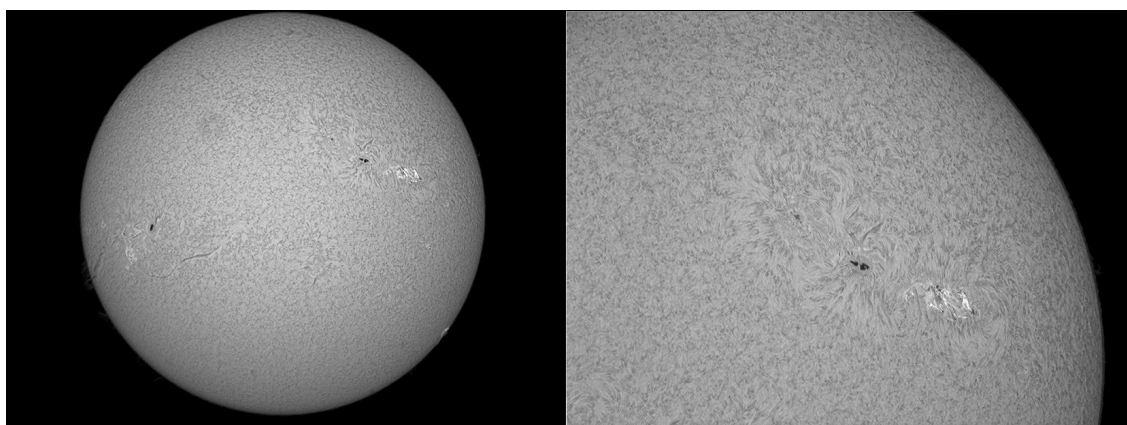


Figure 1. Images of the solar chromosphere in H-Alpha (6562.8 Å) taken in Morelia, Mexico: the whole solar disk (**left**) and the AR 2975 in focus (**right**) on 30 March 2022. The images are provided by the Laboratory of Geo-Spatial Sciences (LACIGE), Morelia, Mexico.

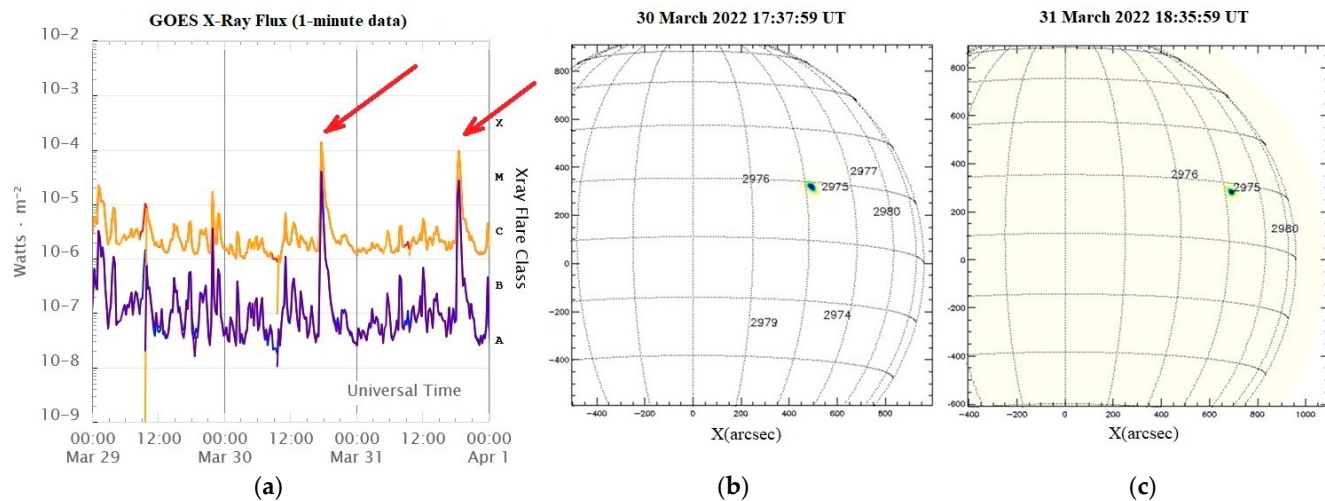


Figure 2. X-ray flux by GOES satellite data (flare moments marked with arrows) (a), and AR position on the solar disk on 30 March 2022 (b) and 31 March 2022 (c). Data supplied by courtesy of SolarMonitor.org and NOAA's Space Weather Prediction Center.

3. Data Used

The ionograms of Vertical Ionospheric Sounding (VIS) taken in the North American low- to mid-latitude sector were used for the analysis. Quasi-vertical ionospheric sounding experimental campaigns were performed in Mexico in 2021–2022. The transceiver and receiver stations were installed in the National Space Weather Laboratory of Mexico (LANCE) in Mexart, Mexico (MEXART, 19.8°N , 101.68°W), and in Morelia, Mexico (IGUM, 19.64°N , 101.22°W), respectively. The distance between the two stations is ~ 51 km. They operated in the range of 2–30 MHz with a frequency sweep rate of 150 kHz/s and a frequency turning step ≤ 1 Hz. The chirp sounding frequency sweep rate and frequency operation range were different in different time intervals and depended on the experiment tasks of the particular time period. During the last days of March 2022, the sounding signal parameters did not change, which allowed us to detect the HF propagation condition variations during the considered flares. We also studied VIS ionograms by the Eglin digisonde station located in the southern part of the US (EG931, 30.5°N , 86.5°W). Eglin ionograms were taken every 7.5 min [23]. Figure 3 shows a map of the experiment.

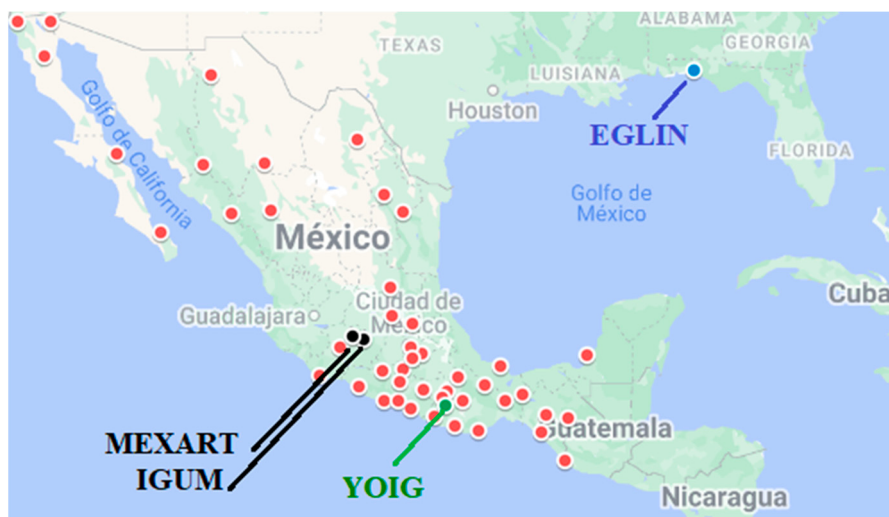


Figure 3. Locations of GNSS receiver stations (red and green circles), ionospheric stations of LANCE equipped with chirp ionosondes (black circles) and the digisonde station in Eglin (blue circle).

Data from 35 local GNSS stations were involved in the analysis (Figure 3). First, based on dual-frequency phase measurements, sTEC values were calculated along each line-of-site (LoS) between the visible GPS satellites and ground receivers. Then, to eliminate trends, the time series of sTEC for every continuous arc (interval when data exhibit no jumps, gaps or other artifacts) were detrended with splines [24]. Third, they were filtered with a centered moving average with three different sets of windows. As a result, we had time series filtered with 2 and 10 min, 10 and 20 min and 20 and 60 min windows. The purpose of filtration is to have variation with periods in the aforementioned ranges. Each of the three time series corresponded to different spatiotemporal scales of ionospheric disturbances. Finally, these three filtered sTEC variations were converted to equivalent vertical variations (dI) for each LoS using the mapping function [25] and references therein. The resulting dI curve is the deviation of the sTEC from its trend. dI is constructed in this way to have its mean values close to zero for every continuous arc. The time series of Rate of TEC index (ROTI) were involved to support the analysis [26,27].

The data on the X-ray and Extreme Ultraviolet (EUV) fluxes measured by the Extreme Ultraviolet Sensor and X-ray Irradiance Sensors at the Geostationary Operational Environmental Satellite (GOES-R) at the geostationary orbit were involved in the analysis [28]. Dst and F10.7 indices were used to estimate the geomagnetic field state and the overall level of solar activity, respectively.

4. Results of Observations

4.1. Flare Effects by VIS Data

4.1.1. Ionospheric Conditions by Ionograms

First, let us consider the ionospheric conditions at the low latitudes of the North American sector (geographic latitude $\sim 20^\circ\text{N}$; geomagnetic latitude $\sim 28^\circ\text{N}$). In March 2022, chirp ionosondes in the center of Mexico were operated in experimental mode. The ionogram background was contaminated with some noise due to radio interference near the receiver station. Nonetheless, the results of observations allowed us to clearly detect the flare effects. It is worth noting that at the end of March 2022, only the traces of reflection from the F2-layer were present on the ionograms during the time of interest (between 17 and 19 UT). We use the observations on 29 March and 1 April as a reference for comparison with the ionograms of 30 and 31 March. The examples of the ionograms for the first flare are shown in Figure 4.

On 30 March 2022, the flare's onset, peak and end were at 17:21, 17:37 and 17:46 UT, respectively. According to the sounding data (Figure 4), a signal amplitude decrease was observed on ionograms beginning from 17:24 UT. The shortwave fadeout (the absence of the reflected signal on the ionograms due to the growth of absorption in the lower ionosphere) was observed between 17:34 and 17:40 UT. Then, the appearance of the signal traces on the ionogram at higher frequencies of the considered frequency range began at 17:40–17:42 UT. The recovery lasted until approximately 18:48 UT, when the pre-flare amplitude level was reached.

To sum up, the lower ionosphere over Mexico (D region and lower part of E region) responded with a 3 min delay to the flare onset. The fadeout lasted about 6 min. The recovery of radio propagation conditions to their pre-flare level lasted about 1 h after the flare end.

Further, we estimate the ionospheric conditions at the middle latitudes of the considered sector (geographic latitude $\sim 30^\circ\text{N}$; geomagnetic latitude $\sim 40^\circ\text{N}$). Since the time step of taking ionograms at the Eglin station is 7.5 min, this complicates the identification of the exact time of the ionospheric responses to fast phenomena. According to the available data (Figure 5), no effect was detected at 17:22:30 UT (1.5 min after the flare onset). The observed signal was less intense and its frequency range shortened at 17:30:00 UT. The reflected signal was absent on the ionogram (fadeout) at 17:37:30 UT (30s after the flare peak) and began to recover at 17:45:00 UT (1 min before the flare end). In general, this timeline is in

accord with the Mexican ionosonde measurements, though the lower temporal resolution of data by Eglin did not allow a detailed comparison

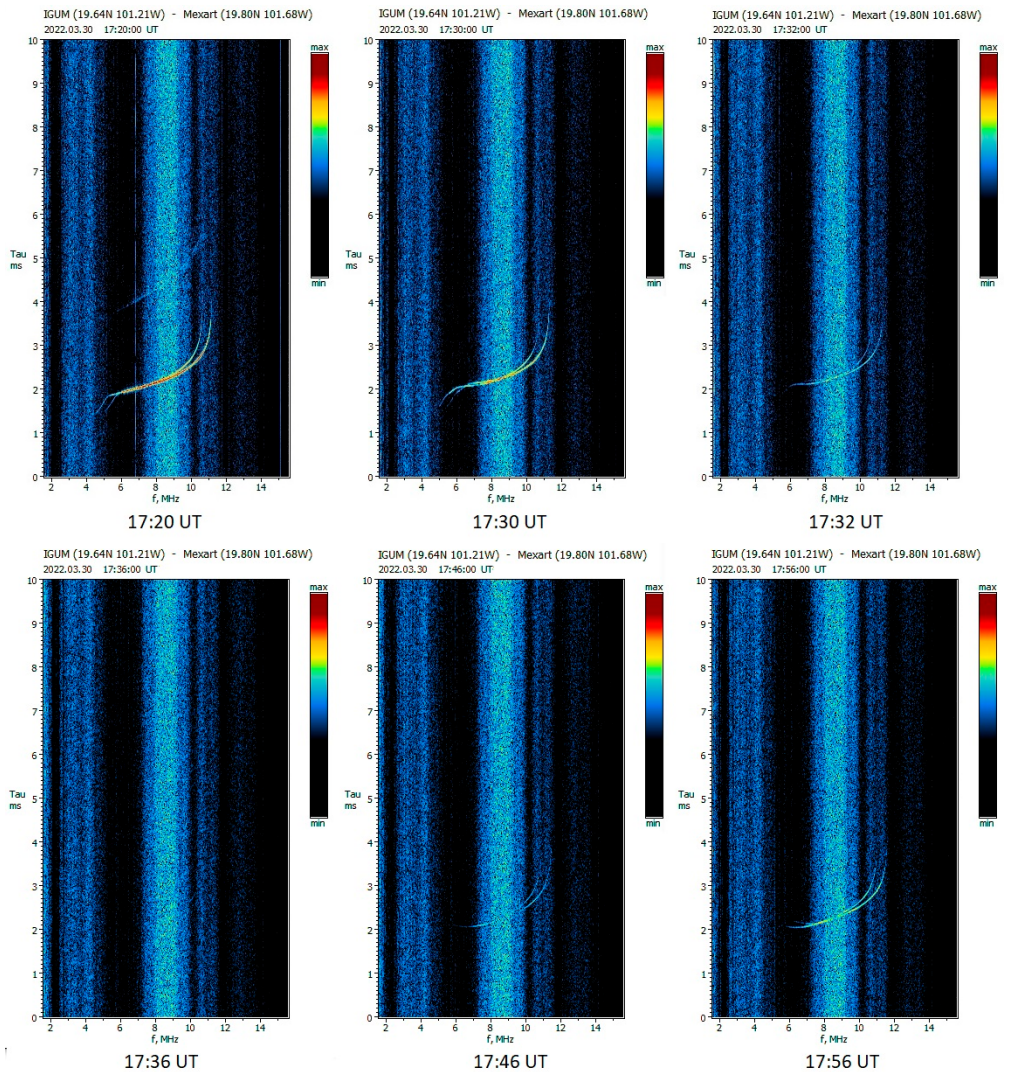


Figure 4. Ionograms taken in Mexico before, during and after the X1.3-flare on 30 March 2022.

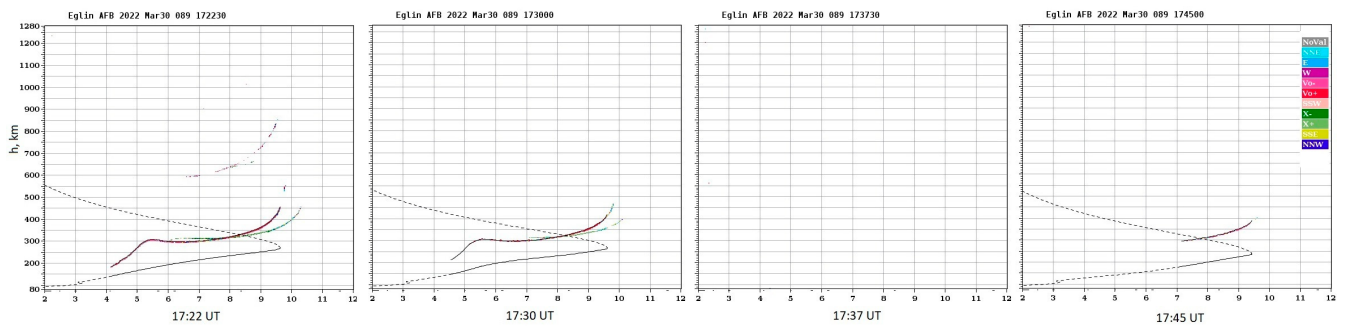


Figure 5. Ionograms taken at Eglin during and after the X1.3-flare on 30 March 2022.

At both stations, the ionospheric response was delayed some minutes after the flare onset. The total absorption of the signal was detected near the time of the flare peak. Here, we note that the sounding signal parameters (emitted power, type of the radio wave (continuous/pulse), antenna pattern, etc.) are different at two stations; therefore, we may

compare the fadeout events only qualitatively. The recovery to the pre-flare conditions was longer at lower latitudes (before the flare end at Eglin and after the flare end in Mexico).

In regard to the less intense flare on 31 March 2022, the beginning of the impact on the lower ionosphere was detected at 18:22 UT (5 min after the flare onset) by the low-latitude VIS data (Figure 6). At 18:28 UT, the narrowing of the frequency range of the reflected signal began. The lowest signal amplitudes and the narrowest frequency range (18:32 UT) were detected 3 min before the flare peak. The recovery of the pre-flare conditions was slow. It began at 18:38 UT and lasted until approximately 19:12 UT. To note, the flare end was at 18:45 UT.

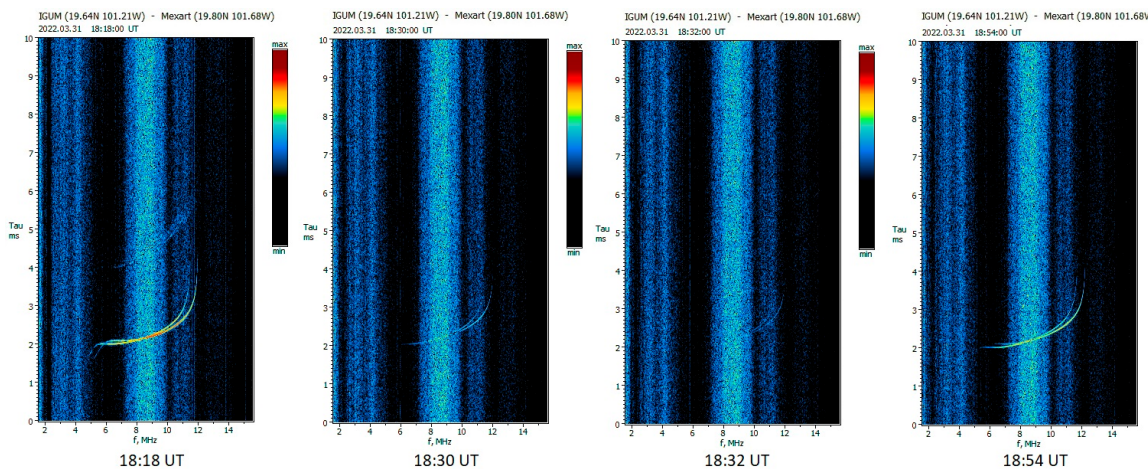


Figure 6. Ionograms taken before and during the M9.6-flare on 31 March 2022.

At the Eglin station (Figure 7), at 18:22:30 UT (5.5 min after the flare onset), still no effect was detected. At 18:30 UT (13 min after the onset), the reflected signal was observed in a very narrow frequency range. At 18:37:30 UT (2.5 min after the flare peak), the range was the narrowest. The recovery to the pre-flare conditions lasted between 18:45 and 19:15 UT (during 30 min after the flare end).

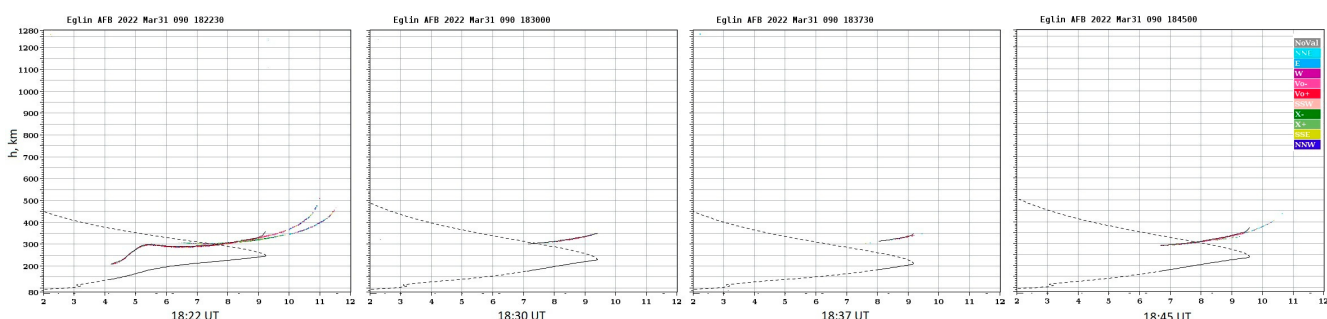


Figure 7. Ionograms taken at Eglin during and after the M9.6-flare on 31 March 2022.

The flare effects at the two stations began simultaneously. In general (as far as the temporal resolution allows estimating), the most pronounced effects and the recovery to the pre-flare HF propagation conditions were also in accord at two stations. In contrast, the day before, the responses in Mexico and Eglin to the more intense flare were not so synchronized (the effects in Mexico lasted longer). The illumination conditions (LT of the flare) at Mexican and Eglin meridians were more similar on 31 March than on 30 March. In this case, the longitudinal difference between the stations was more important than the latitudinal difference. The difference in the ionospheric response in Mexico and Eglin on 30 March is probably explained by the different Sun's zenith angle at the moment of the flare.

To sum up, according to the low-latitude ionosonde data of 2 min time resolution, the effects of the X1-flare lasted ~1 h 24 min. The effects of the M9-flare on the next day lasted ~40 min. In both cases, the effect duration was longer than the flare duration (in contrast to the effects in the F2 region and topside ionosphere by GNSS data, as shown further).

A detailed comparison of the flare impact processes with time is given in Figure 8. The more intense (X1.3) flare on 30 March provoked the more significant response (narrowing of the operation range and the signal amplitude decrease on ionograms) in the lower ionosphere of the low- to mid-latitude North American sector than the less intense (M9.6) flare on 31 March. Though, from first glance, this conclusion seems obvious, it is not obvious at all. There are important factors other than the X-class of the flare. For instance, Barta et al. [7] emphasized the role of the solar zenith angle.

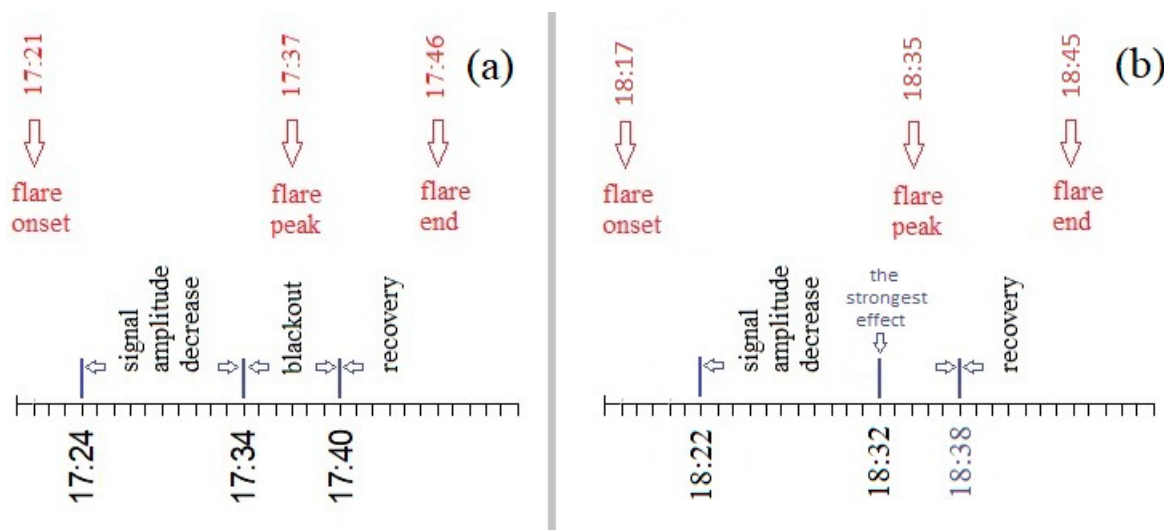


Figure 8. Timeline of the ionospheric response by the ionosonde data: X1.3-flare (a) and M9.6-flare (b).

4.1.2. Estimation of the Reflected Signal Attenuation in Mexico

Ionograms provide many ionospheric and radio propagation parameter values. One approach is to study the amplitude of the received ionospheric sounding signal (e.g., [8]). In our case, the relative amplitude of the reflected chirp signal is displayed on ionograms with color (color bar in the right part of the ionogram). When measurements are performed with the same transceiver settings (no changes of the sweep rate, emitted power, frequency and delay ranges, ionogram width, etc., during the period of interest), these amplitudes (dB) in a series of ionograms may be compared to each other. A qualitative assessment of the relative amplitudes of the received signal was obtained during the flares for the following cases.

(1) The assessment of the relative signal amplitude (A) at the critical frequency of the F2 layer for ordinary ($foF2$) or extraordinary ($fxF2$) components does not seem possible, as the trace of the signal at these frequencies was not observed well or was absent on several ionograms due to the increased absorption. Therefore, for each ionogram, we analyzed the maximal A without regard to the frequency at which this maximal A was observed. Since this frequency was different on each ionogram, our assessment is only of a qualitative character. Nevertheless, further analysis showed the validity of this approach.

(2–3) Estimation of the signal amplitude at the same particular frequency is not always possible, as the position of the traces on the ionograms changes with time (even under quiet conditions). We analyzed A (dB) at 7 and 11 MHz because in our case, the reflected signal was always present at these frequencies, with the exception of the fadeout interval.

For all three cases mentioned above, the relative amplitudes on the last ionogram taken before the flare onset were considered as the reference amplitudes. Then, the difference between the reference values and the values of amplitudes observed on the subsequent

ionograms (taken after the flare onset) were calculated. Figure 9 shows the results for cases (1)–(3) described above for three time intervals—that is, during the X1.3-flare of 30 March and during the M9.6-flare of 31 March. As the time resolution of VIS data for 29 March does not allow us to perform comparison with this quiet day, the day after the second flare was chosen for comparison. The curves for 1 April are shown only during the time interval of the first flare (30 March). Variations on 1 April during the same time interval as for the second flare (31 March) are not shown for the economy of space. Essentially, they were rather similar to the variations shown in Figure 9c. We remark that 1 April may not be considered a geomagnetically quiet day, but it may be used as a reference day, first, because the time scale and the magnitude of the ionospheric response to flares and magnetic field disturbances are different and, second, because here, we compare the relative amplitudes of the signal that are affected by flares and not affected by geomagnetic disturbances.

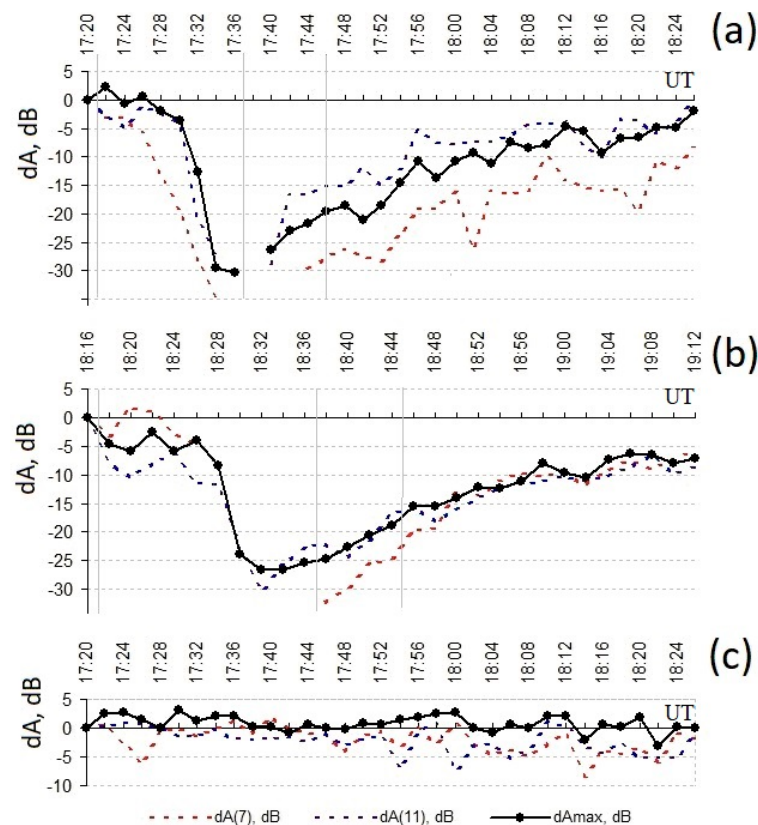


Figure 9. Deviation of the maximal relative amplitudes of the signal observed in ionograms during the intervals of the flares on 30 March (a) and 31 March (b) and for the reference day, 1 April (c). Thin gray vertical lines indicate the moments of the flare onset, peak and end.

Figure 9 illustrates the flare impacts: the decrease of the received signal amplitude by 27.28 dB (at 11 MHz) was detected 13 min after the solar flare onset on 30 March. This decrease was immediately followed by the fadeout event (~15 min after the flare onset). As for 31 March, the maximal amplitude decrease by 30.38 dB (at 11 MHz) was revealed 14 min after the flare onset. During the reference day of 1 April, the relative amplitude deviation did not exceed the value of 7 dB.

To conclude, the maximal impact of the flare on the reflected chirp signal amplitude in the center of Mexico was observed approximately 14–15 min after the flare beginning for both considered flares.

4.1.3. Correlation with Different Ranges of EUV and X-ray Radiation

The solar radiation spectral composition qualitatively changes during flares. The flare impact on the ionosphere depends on the amount of radiation emitted in different EUV

and X-ray ranges. To estimate the change of the absorption level during the flares, we considered deviation of the relative amplitude of the reflected signal on the ionograms (dA) discussed in the previous section. In addition, the value of the minimal frequency at which the signal traces were observed on the ionogram (f_{min}) was considered. This parameter is mainly defined by the absorption level in the ionosphere.

The linear correlation coefficients (r) between the time series of dA and EUV/X-ray fluxes within different frequency bands were calculated. As the time step of ionograms was 2 min, the time series of EUV and X-ray fluxes were also reduced to this step. Please note that the series lengths were not the same as sometimes the signal trace was absent at some frequency or at all frequencies due to absorption. Nonetheless, this analysis allows us to obtain at least a qualitative assessment of the impacts of different radiation bands. The coefficient r was also calculated between the f_{min} value and the EUV/X-ray fluxes within different frequency bands. The results for the two flares are presented in Tables 2 and 3. Low r values are given in red and high r values in blue.

Table 2. The coefficient r during the X1.3 flare.

EUV Bands, 30 March 2022						
	25.6 nm	28.4 nm	30.4 nm	117.5 nm	121.6 nm	133.5 nm
$dA(7)$, dB	−0.75	−0.65	−0.85	−0.70	−0.79	−0.76
$dA(11)$, dB	−0.82	−0.54	−0.86	−0.89	−0.74	−0.91
dA_{max} , dB	−0.90	−0.73	−0.97	−0.86	−0.91	−0.90
f_{min}	0.89	0.52	0.92	0.95	0.80	0.96

Table 3. The same as in Table 2, but for the M9.6-flare.

EUV Bands, 31 March 2022						
	25.6 nm	28.4 nm	30.4 nm	117.5 nm	121.6 nm	133.5 nm
$dA(7)$, dB	−0.91	−0.54	−0.93	−0.67	−0.81	−0.82
$dA(11)$, dB	−0.76	−0.07	−0.82	−0.84	−0.67	−0.91
dA_{max} , dB	−0.83	−0.19	−0.88	−0.83	−0.76	−0.91
f_{min}	0.63	0.03	0.66	0.68	0.52	0.73

For the more intense flare, there is a rather strong correlation between the EUV radiation bursts and the change of the amplitude of the received sounding signal (Table 2). The effect was much less pronounced for the less intense flare (Table 3). In general, according to the data of both flares, the lowest or even absent correlation was observed between the absorption level (represented by the signal amplitude and f_{min}) and the emission in the 28.4 nm spectral band. The highest correlation was observed in the case of the 133.5 nm band, meaning the strongest impact on the lower ionosphere was caused by this EUV spectral band.

Figure 10 schematically shows the EUV flux variation for different bands: the values for each curve were multiplied by a coefficient k (different for each band) to adjust all the curves to a similar scale. This was done for illustrative purposes to compare the forms of the curves. Black curves with dots show the f_{min} values along the right Y-axis. It results that the increase of the emission in the 28.4 nm band (second curve from the top of the figure) was less abrupt in contrast to other spectral bands. This may explain why its effect on the absorption level was less pronounced.

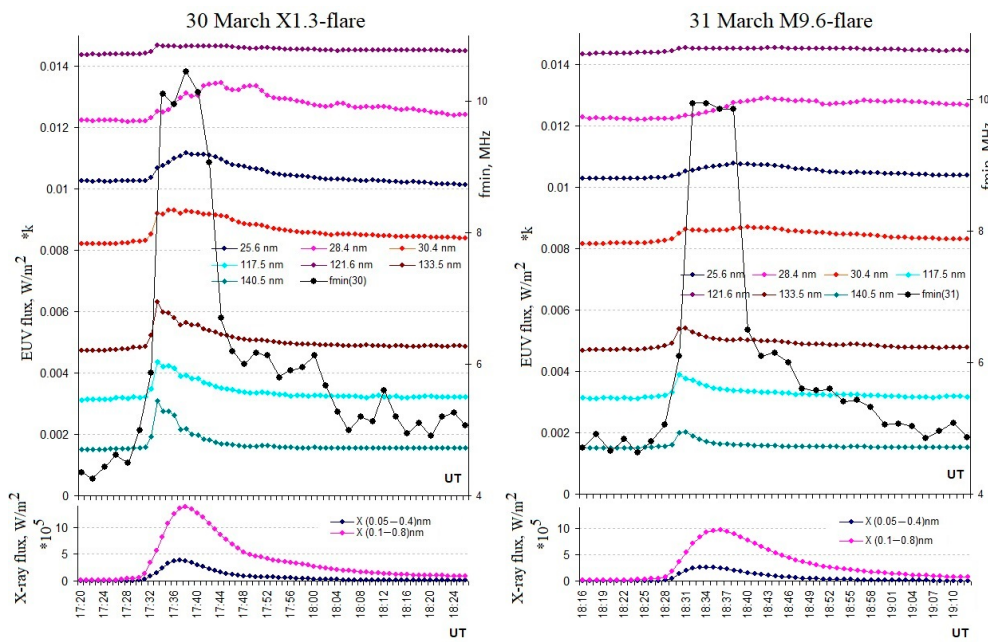


Figure 10. Schematic representation of the EUV and X-ray fluxes in different spectral bands (left Y-axis) and the corresponding f_{min} variation (right Y-axis) for the periods of X1.3-flare (left) and M9.6-flare (right). EUV flux value is given in the form of $\text{EUV} \times k$, where k is the specific coefficient for each band (from top to bottom k values are 80; 130; 15; 30, 1.75; 20; 10). The X-ray flux value is given in the form of $\text{EUV} \times 10^5$.

It was even more interesting to study the same correlation but with the X-ray spectral bands, as it is known that the physical source of strong increases of electron concentration in the ionospheric D region during flares is the X-ray radiation in the wavelength range shorter than 10 nm. The results are shown in Tables 4 and 5. X-ray variations are shown in Figure 10.

Table 4. The same as in Table 2, but for X-rays.

X-ray Bands, 30 March 2022		
	(0.05–0.4) nm	(0.1–0.8) nm
dA(7), dB	-0.8	-0.84
dA(11), dB	-0.91	-0.88
dAmax, dB	-0.89	-0.93
fmin	0.96	0.92

Table 5. The same as in Table 3, but for X-rays.

X-ray Bands, 31 March 2022		
	(0.05–0.4) nm	(0.1–0.8) nm
dA(7), dB	-0.93	-0.95
dA(11), dB	-0.9	-0.89
dAmax, dB	-0.93	-0.94
fmin	0.96	0.91

At first glance, it seems that the X-ray radiation within the shorter wavelengths (between 0.05 and 0.4 nm) had more effect on the f_{min} variations. At the same time, such a conclusion may be incorrect. Considering the qualitative character of our assessment

and the fact that, in general, r in Tables 4 and 5 varies near the values of high correlation (0.8–0.95), we consider it impossible to make conclusions about which of the X-ray bands had a more pronounced impact on the absorption level in the lower ionosphere. The only conclusion from Figure 10 and Tables 4 and 5 is that the role of the X-ray radiation during the flares is the most important, which coincides with the well-known fact from the literature.

To conclude, the major role of the X-ray radiation in the electron concentration increase in the lower ionosphere of the considered region during the flares was confirmed. As for the EUV radiation impact on the lower ionosphere, it cannot be totally discarded. It was more pronounced for the more intense flare X1.3 than for M9.6. For the particular cases of the two considered flares, the EUV emission in the 28.4 nm spectral band provoked the weakest impact on the absorption conditions in the lower ionosphere (probably due to the smooth gradual increase of radiation in this band) and the 133.5 nm band had the most pronounced impact. Therefore, the parts of the spectrum that have the greatest influence in this case have been identified.

4.2. Flare Detection by GNSS Data

4.2.1. Features of dI Response

We considered sTEC variations that were filtered with a moving average of different windows (see Section 3). Due to the time scales of the ionospheric responses to the flares and the duration of these responses, the most informative data were the dI time series obtained with (2–10) min and (10–20) min windows. Some traces of responses were also detected in the dI(20–60) min series, but they were detected only at some LoSs and mostly did not exceed the background dI(20–60) fluctuations. To add, this filtering did not allow us to estimate adequately the time of the dI response because of its duration being less than 20 min. To discard the possible dI peaks caused by the multipath effects of GNSS signal reception, the dI data were analyzed not only during the flare day but also the day before (for comparison).

dI variations were studied at each LoS from different satellites. Figure 11 illustrates an example of dI(2–10) variations observed at the receiver station YOIG in the south of Mexico (Figure 3). A certain pattern of dI behavior was detected at all LoSs during the flare: the dI(2–10) decrease after the flare onset followed by the moderate increase and then, before or at the moment of the flare end, the return to the level of the background variations. The only different pattern is seen for the ray path YOIG-G07. Probably, it is explained by the local processes that were not overcome by the flare effect. The analysis of Figure 11 shows that the dI(2–10) variation caused by the flare was of a small amplitude compared with other effects, which, for example, are seen at LoSs YOIG-G09 and YOIG-G06 at 18:30 UT. These were provoked by the multipath effect due to some obstacle in the signal path. Another conclusion is the simultaneity of the dI response at all LoSs.

Let us describe the responses to each flare, as it is known that they can vary. For example, based on data for X-, M- and C-flares during 2014–2017, Syrovatskiy et al. [29] demonstrated that the response to a flare with a sufficiently strong X-ray flux may practically not manifest itself, and vice versa, the response to a weaker flare may turn out to be greater than to a stronger flare. Dmitriev et al. [15] also discussed the issue of why a weaker flare can produce a larger TEC enhancement and a very intense flare can produce effects comparable to those caused by moderate flares. These facts prove the presence of variability in the ionospheric response. The flare intensity defined in terms of the X-ray class of the flare may not be a measure of the ionospheric response in the F2-region [20,30,31].

Figure 12 shows examples of dI(2–10) and dI(10–20) variations for 30 March 2022 at LoSs from satellites G14 and G30 to different receivers. dI curves during the flare were characterized by the II-form: the negative bay followed by the positive peak. The same dI behavior pattern was revealed at all LoSs for this day (not shown for the economy of space). Notwithstanding the small amplitudes of dI deviations, the simultaneity and uniformity

of the response at all LoSs, as well as the moment of the ionospheric response occurrence, leave no doubt that it was caused exactly by the flare.

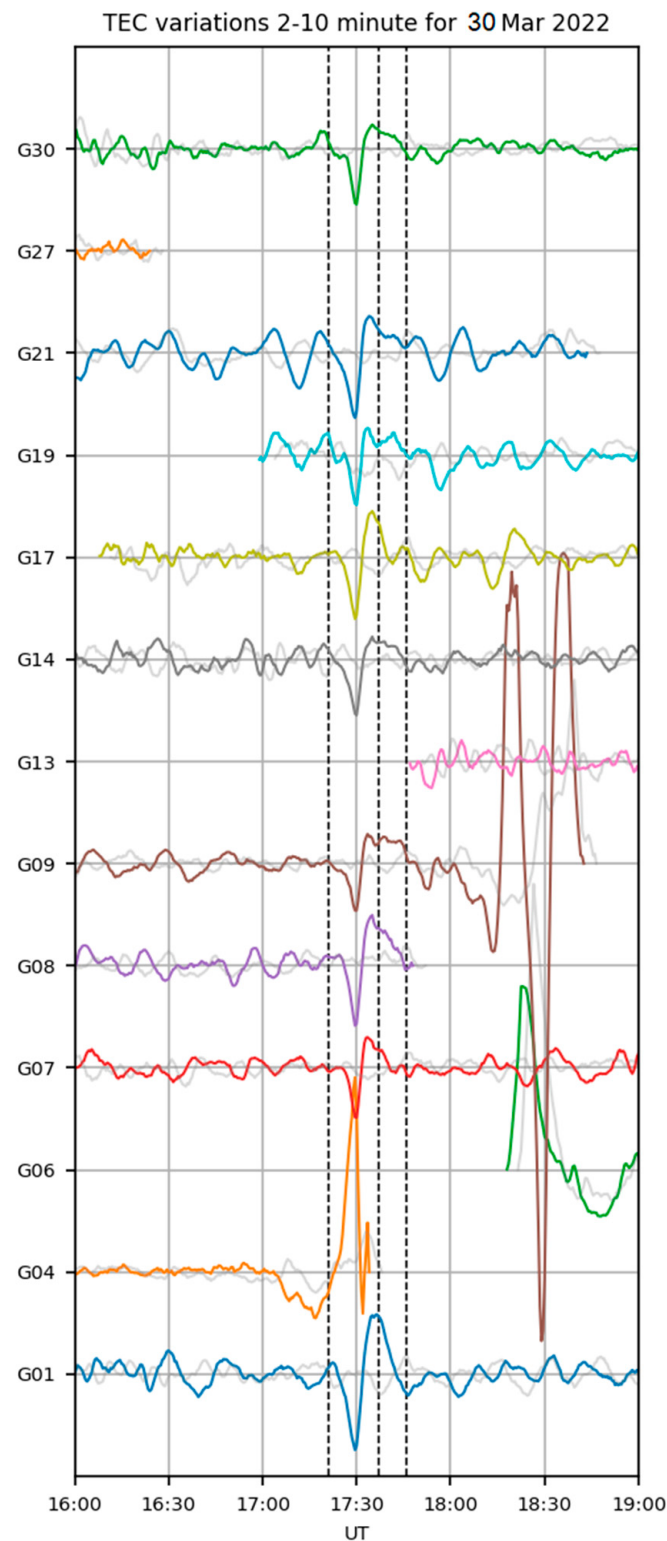


Figure 11. di(2–10) variations registered at the YOIG station on 30 March 2022. Each curve represents the di(2–10) for the corresponding GPS satellite. The Y-axis unit is 0.3 TECU. The dashed lines mark the flare onset, peak and end. Colored di curves stand for the day of the flare and the gray curves stand for the day before (for comparison).

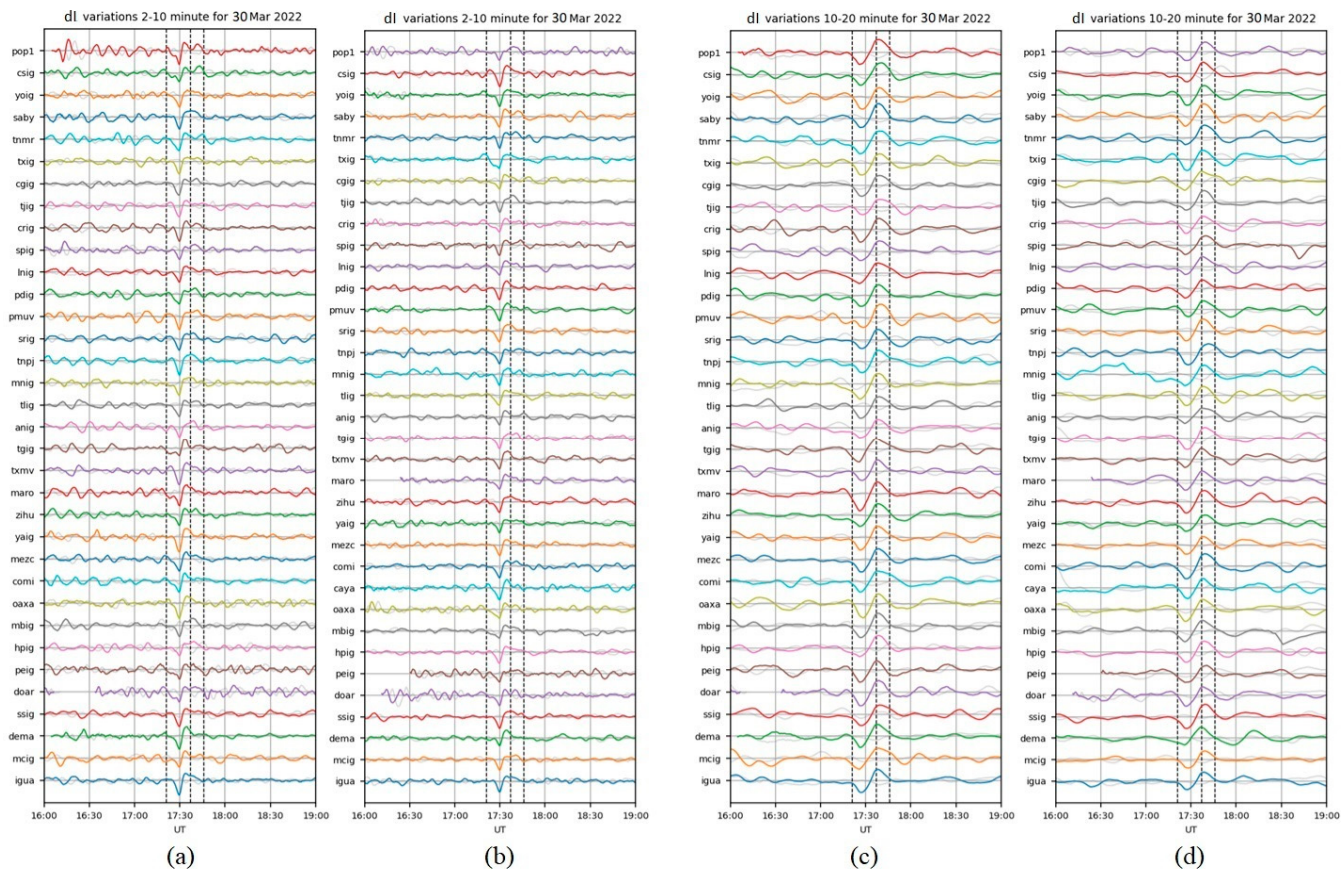


Figure 12. di(2–10) variations at LoSs to satellites G14 **(a)** and **(b)** G30 and di(10–20) variations at LoSs to satellites G14 **(c)** and **(d)** G30 for the case of X.3-flare on 30 March 2022. The Y-axis unit is 0.3 TECU. The dashed lines mark the flare onset, peak and end. Colored di curves stand for the day of the flare and the gray curves stand for the day before for comparison.

In the case of the less intense flare of 31 March 2022 (Figure 13), the di response at many LoSs did not exceed the level of background fluctuations. In general, the response (when detected) was less intense than in the previous case. It can be noted that sometimes di(2–10) show the II-pattern but at the same time, the deviations are of the same amplitude as the background fluctuations. Only the simultaneity of the II-form occurrence indicates that it is a response. As for the di(10–20) variations, the response was not present at some LoSs. When it was present, the parameter deviations exceeded the background fluctuations. At the majority of LoSs (please note that only the examples are shown in Figure 13), the negative bay in the temporal di (10–20) variations was more pronounced than the following positive peak.

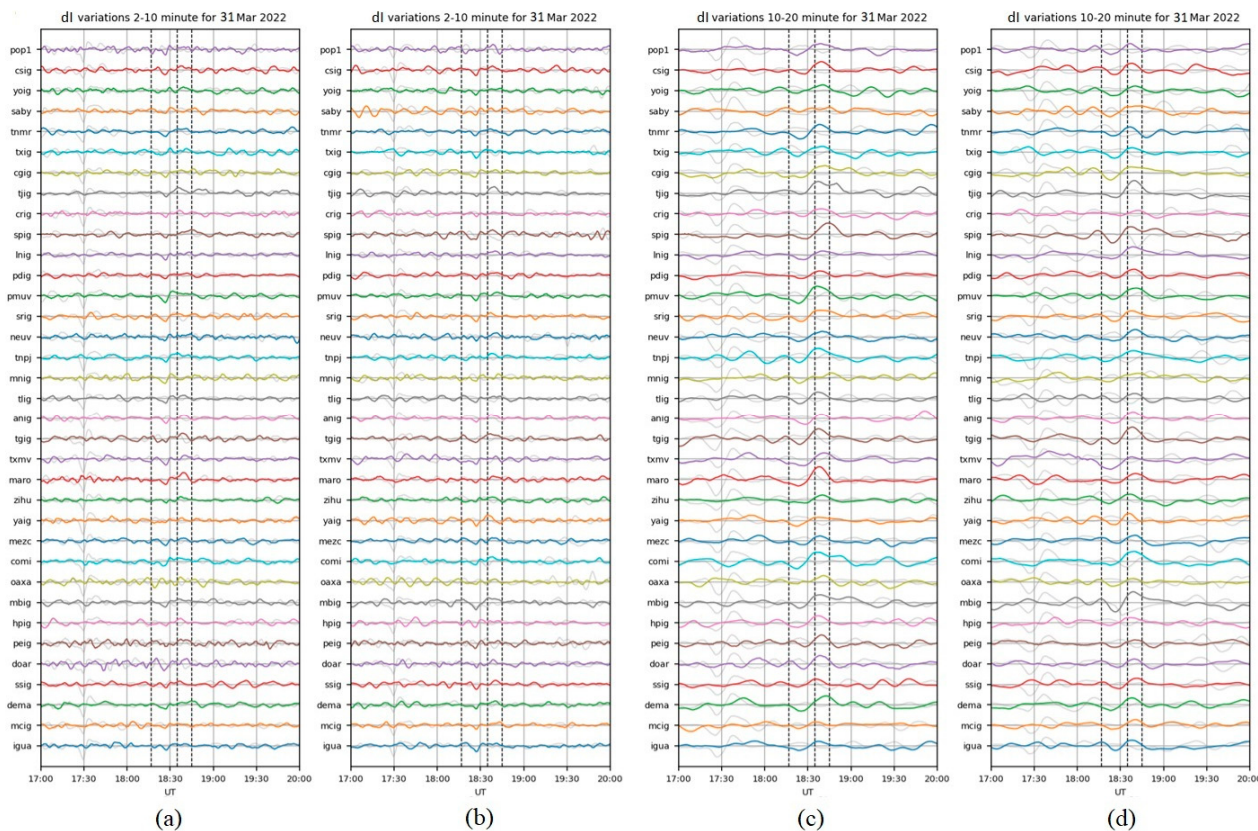


Figure 13. di(2–10) variations at LoSs to satellites G14 (a) and (b) G30 and di(10–20) variations at LoSs to satellites G14 (c) and (d) G30 for the case of X.3-flare on 31 March 2022. The Y-axis unit is 0.3 TECU. The dashed lines mark the flare onset, peak and end. Colored di curves stand for the day of the flare and the gray curves stand for 30 March 2022.

Considering the general small amplitude of di variations, we constructed the maps of the sub-ionospheric points at all LoSs before, during and after the flares as it results that such a representation of results allows us to better appreciate the flare effects on di. The maps of the sub-ionospheric points were constructed with a time step of 30 s. The examples are given in Figure 14. Essentially, the green color of the points means no deviation of di(10–20) over this point; the blue color means negative and the red color means positive deviation. The animation of the sequence of maps is available as Supplementary Materials to this article (<https://zenodo.org/record/7363050>, accessed on 25 December 2022).

There are different works dedicated to the roles of position of AR responsible for the flare, solar zenith angle at the moment of the flare and flare X-class in relation to the ionosphere response to the flare [18] and references therein. According to the literature, the impact of X-ray radiation during flares does not depend much on the flare's AR position on the solar disk. In contrast, EUV radiation during flares is more geo-effective if the corresponding AR is in the center of the solar disk [32,33]. Therefore, the smaller effects of the M9.6-flare on the lower ionosphere may be explained by the weaker X-class of the flare and on the F2 layer and topside ionosphere, at least partially, by the AR position, which was further from the solar disk center than during the X1.3-flare. The issue of the influence of the solar zenith angle on the ionospheric response was discussed by different authors, for example [2,10,30,31]. In our case, the solar zenith angle in the center of Mexico was $Z(\text{sun}) = \sim 26^\circ$ during the first flare and $Z(\text{sun}) = \sim 17^\circ$ during the second flare, meaning that in the second case the $Z(\text{sun})$ conditions were more favorable to cause the major effects, as it was closer to the noon. However, smaller di deviations were registered during the second flare. Considering the similarity of the other observation conditions (Table 1), this implies that the ionospheric response depended more on the AR position and the flare class

than on the solar zenith angle. Nevertheless, this is the preliminary conclusion, as more statistics is needed.

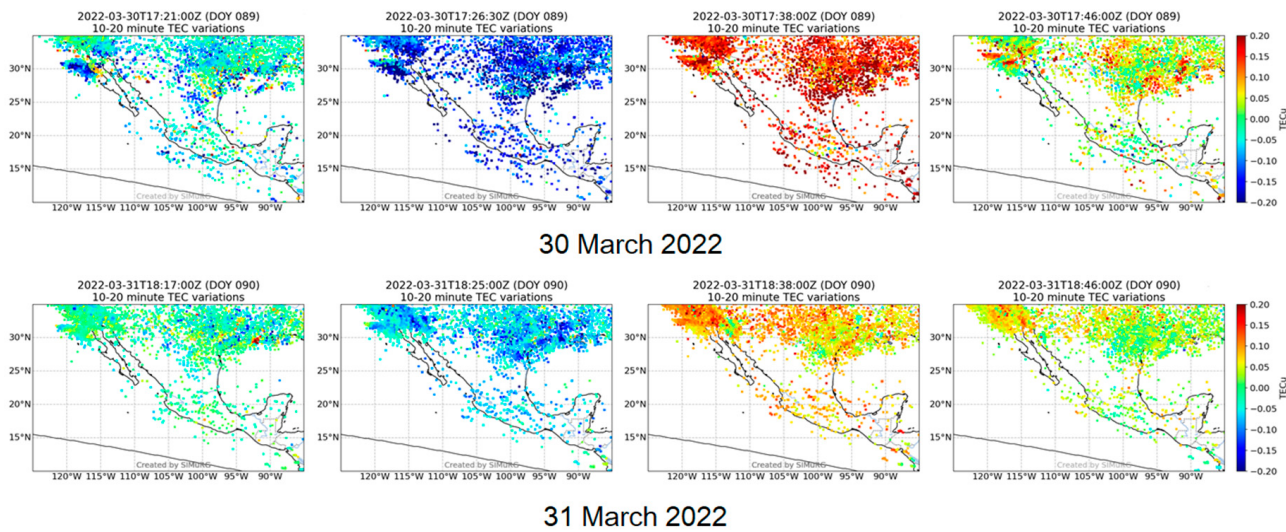


Figure 14. Maps of sub-ionospheric points over Mexico for 30 March 2022 (**upper panels**) and 31 March 2022 (**lower panels**). Deviations of DI(10–20) are represented by the color of each point. The maps are shown for the following moments from left to right: flare onset, major negative deviation, major positive deviation and flare end.

The presence of the negative bay in the DI variation (I-form) can be a result of either the sTEC filtering procedure or the physical effect. There are works that evidenced negative TEC deviations during flares. For example, Thome and Wagner [34] reported negative disturbances (3–10%) within heights of 280–600 km as a response to two flares. According to the simulation results by Leonovich and Taschilin [35], the electron concentration decrease in the outer ionosphere can be caused by O⁺ ion outflow towards the plasmasphere. After the “switching off” of a flare, the plasma pressure in the F2 region decreases rapidly and the difference in pressure between the upper and lower ionosphere cannot maintain O⁺ ion flow in the upward direction. The ionosphere returns to its undisturbed state [35]. There are more works on this issue. Mendillo and Evans [5] reported such an upward outflow caused by flares. Mendillo et al. [16] showed that an enhancement of upward plasma flux occurs for large flares observed on Earth. To provide a more recent example, Liu et al. [19] studied the ion upflow near the X9.3-flare peak on 6 September 2017 and found that ambipolar diffusion enhancement is the main driver for it. The last mentioned work also provides a list of references for different mechanisms proposed to explain the ionospheric upflow in the literature. In addition, the reader can find a list of publications on the dynamics resulting in the ionospheric outflow of O⁺ ions in work by Lin and Ilie [36]. From the other hand, Yasyukevich et al. [22] applied the same methodology as in the present work to study solar flare effects during September 2017. According to these authors, as the filtering results in a zero mean value, any DI increase is shown as a decrease with the minimum at the moment of the event onset. In our case, the DI minimum was between the flare onset and the rapid increase of radiation to its peak during the flare. Additional studies are needed, especially since the processing methods used by different authors are different. To verify the “physical” version in our case and to study the ion/electron behavior exactly in the F2 ionospheric layer and/or higher, low-orbit data are needed. Unfortunately, no satellite with the necessary data passed over the North American low-latitude region at the moments of the flares. Therefore, we cannot draw a definitive conclusion on this issue. According to the ionograms, foF2 did not show (short-term) rapid large deviations, which means there was no much change in the electron concentration during the flares at the F2 layer heights. Although foF2 had some decrease after the first flare onset, it was very small (~1% of the value). In addition, it should be noted that the foF2 values showed significant day-to-day

variability. Basically, short-term foF2 variations before, during and after the flares on 20 and 31 March 2022 did not seem different from the background fluctuations during the same period on the reference day of 1 April. Therefore, it can be inferred that the detected dI response was a result of changes at the higher altitudes, as it is known that the ionospheric regions above the F2 layer can contribute, by various estimates, up to 25–30% of the TEC value (e.g., [37]). Mendillo et al. [10] studied the TEC response to the great flare with data from North America, Europe and Africa and also emphasized the role of the changes above the F2-layer peak height.

Furthermore, due to the application of moving average as a filter to the dI time series, it is difficult to estimate the real duration of the effects in the ionosphere. In this regard, for both flares, the characteristic coincidence of the phases of dI(10–20) variation and flare phases was noted. First, at the moment of flare onset, dI(10–20) began to decrease and further to increase. The increase was maximal at the moment of the flare peak. Then, the dI(10–20) value decreased to its pre-flare value. This recovery ended at the moment of the flare end (examples given in Figures 11 and 12). The described pattern seems interesting and may not be ignored. We will proceed from the assumption that dI(10–20) are closer by their time scale to the duration of the sTEC response to the flares.

4.2.2. Correlation with Different Ranges of EUV and X-ray Radiation

The assumption that the response of the ionosphere in the F2 region and above depends on the particular level of radiation in different EUV spectral bands was made previously in several classical [1,13] and more recent works [16]. It would be interesting to estimate, at least qualitatively, their impacts on the dI change. Similar to Section 4.1.3, the coefficient r was calculated between the time series of dI and EUV and the X-ray fluxes of different spectral bands. The 30 s dI series were adjusted to 1 min GOES data. It was shown that the dI response at different LoSs was of the same pattern; consequently, it was sufficient to calculate r for the parameters only at one LoS. For this purpose, the time series of dI(2–10), dI(10–20) and ROTI at the ray path between the GPS satellite G17 and YOIG station (considered before) were used for the analysis. We recall that dI(2–10) corresponds to irregularities of the small scale and dI(10–20) to those of the medium scale. ROTI was involved as an additional parameter to better understand dI variations because it is always positive, which may be useful to identify the beginning of the ionospheric response. The length of the time series was limited by the flare duration because (as shown above) the dI variations are not exclusively affected by flares. They can present other features over a longer period. The results are presented in Tables 6 and 7. Considering the overall strong dependence of the ionosphere behavior on solar radiation as well as the fact that the fluxes of UV and soft X-rays at wavelengths correlate with each other, for our particular case we consider correlation to be strong if $r \geq 0.9$ and moderate if $0.7 \leq r \leq 0.9$.

Table 6. Correlation between sTEC derivatives and fluxes of different spectral bands during X1.3-flare.

r (17:20–17:46 UT)	EUV 25.6 nm	EUV 28.4 nm	EUV 30.4 nm	EUV 117.5 nm	EUV 121.6 nm	EUV 133.5 nm	EUV 140.5 nm	X (0.05–0.4) nm	X (0.1–0.8) nm
dI(2–10)	0.60	0.39	0.63	0.65	0.59	0.60	0.58	0.64	0.58
dI(10–20)	0.93	0.74	0.87	0.71	0.84	0.70	0.51	0.93	0.93
ROTI	0.51	0.17	0.68	0.92	0.63	0.90	0.95	0.54	0.43

Table 7. The same as in Table 6, but for M9.6-flare.

r (18:16–18:45 UT)	EUV 25.6 nm	EUV 28.4 nm	EUV 30.4 nm	EUV 117.5 nm	EUV 121.6 nm	EUV 133.5 nm	EUV 140.5 nm	X (0.05–0.4) nm	X (0.1–0.8) nm
dI(2–10)	0.54	0.59	0.65	0.51	0.66	0.58	0.46	0.34	0.40
dI(10–20)	0.97	0.91	0.95	0.50	0.91	0.64	0.31	0.73	0.87
ROTI	−0.44	−0.44	0.51	−0.54	−0.59	−0.58	−0.50	−0.34	−0.35

In general, during the more intense X1.3-flare correlation between the dI series filtered with the (10–20) min window and the fluxes of all spectral bands was rather high. Radiation at 25.6 nm had the major impact on dI(10–20). Surprisingly (as EUV is known to play the main role in the higher ionosphere), X-ray flux of both shorter and longer wavelengths showed a strong correlation with dI(10–20) (of the same level as EUV at 25.6 nm). Correlations for dI(2–10) were mostly weak. Correlations for ROTI were strong to 117.5, 133.5 and 140.5 nm and almost absent for other bands. In general, r for the 28.4 nm band (see Figure 14 upper panel) was rather low (similarly to the lower ionosphere). This was probably due to the more gradual increase at this wavelength.

Figure 15 (upper panel) illustrates the sTEC derivative variations from Table 6 and the bursts of radiation in the chosen bands. Similar to Figure 10, EUV and X-ray flux values are multiplied by the specific coefficient for each band (coefficient values are not listed as they have no physical meaning) for illustrative purposes. Both dI(2–10) and dI(10–20) increases to their peak values occurred with the flux intensification at the mentioned EUV bands and the corresponding X-ray burst. The beginning ROTI increase corresponded to an increase of X-rays as well. At that, we should note that due to the rules of ROTI calculation, there is an uncertainty of its peak beginning within a 5 min interval. This probably explains why ROTI and dI(2–10) response beginnings are not synchronized in the upper plot of Figure 14. If the ROTI curve is “moved” 4 min to the left on the X-axis, its response beginning will correspond to a dI(2–10) decrease.

Positive dI(2–10) and dI(10–20) manifested themselves with the EUV flux increase at particular wavelengths (dotted curves). Negative dI bay is seen after the onset of the flare at 17:21 UT before the peaks of radiation at different bands. It is worth noting that the flare onset is defined as the first minute in a sequence of 4 min of the monotonic increase in (0.1–0.8) nm flux. The fact that the transition from negative to positive dI occurs exactly at the moment of the solar radiation’s rapid increase to its peak calls attention. Maybe, it suggests that during the slow increase of radiation, a certain process is responsible for the dI decrease and then, during the rapid growth of radiation, another process (ionization) begins to dominate in the dI behavior. Still, as if there is no certainty that the dI transition from negative to positive values has a physical meaning.

As for the less intense flare on 31 March, it was shown that it provoked mostly medium-scale irregularities. This is confirmed by the results in Table 7: only correlations for dI(10–20) are worth noting. ROTI did not show any response in this case. In contrast to the more mixed influence during the more intense flare, EUV bands that impacted more can be clearly revealed. In particular, the 25.6, 28.4, 30.4 and 121.6 nm spectral bands showed strong correlation with the ionospheric response. Radiation at 25.6 nm played a major role (very strong correlation, $r = 0.97$). Similar to the previous case, negative dI are observed after the flare onset and the transition from negative to positive dI occurred exactly at the moment of the beginning of the radiation bursts. In addition, we recall that during M9.6, the positive dI(10–20) were rather weak at some LoSs (probably due to the less intense radiation), but the negative dI(10–20) bays were well detected.

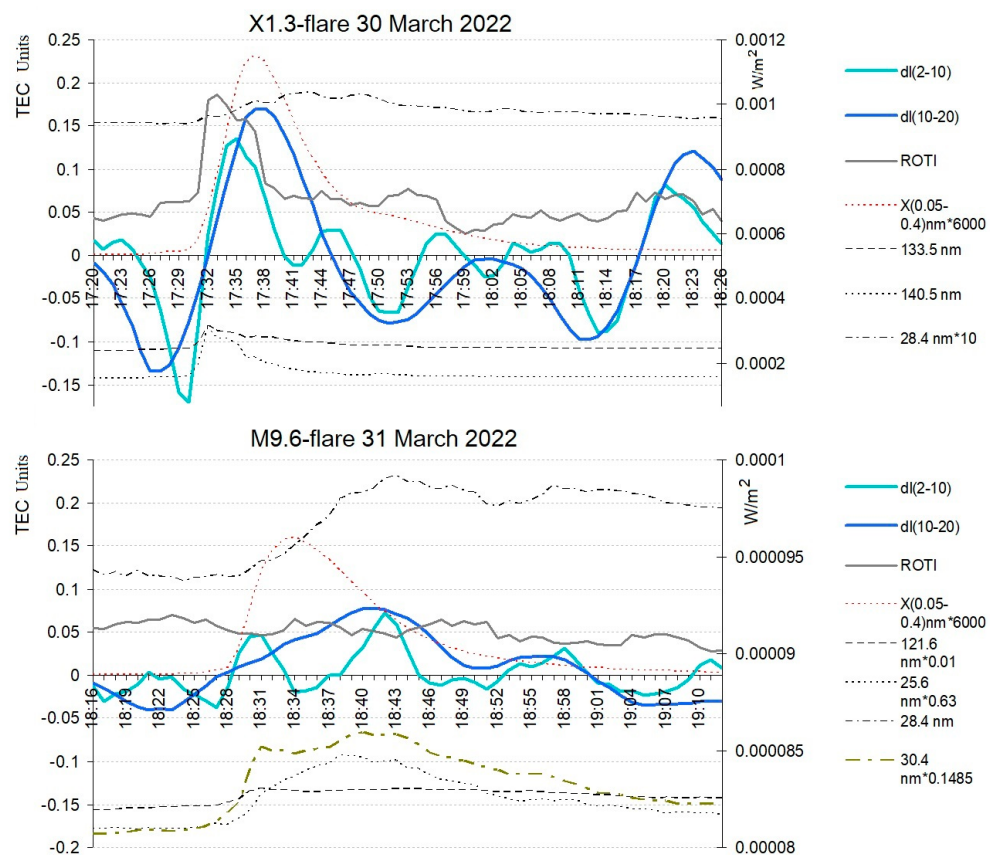


Figure 15. di variations filtered with the windows (2–10) and (10–20) and ROTI variations (continuous curves) during the X1.3 flare on 30 March 2022 (**upper panel**) and the M9.6 flare on 31 March 2022 (**lower panel**). Dotted lines schematically show the bursts of solar radiation in the chosen spectral bands.

It was shown previously that the flare impact on the ionosphere depends on the amount of radiation emitted in different EUV and X-ray bands [11,19,35,38]. Figure 5 in [37] shows an interesting picture of how increases in different solar radiation spectral intervals influence the contribution of different ionospheric regions (heights) to the TEC value. According to these authors, the electron content increase in the topside ionosphere is related to EUV spectral bands of 55–65 and 85–95 nm. Berdermann et al. [11] stated that the EUV component around 30 nm can seriously affect GNSS positioning services. According to Hernández-Pajares et al. [38], vertical TEC is highly correlated with EUV photon flux at the 26–34 nm spectral band, which is geo-effective in the ionization of mono-atomic oxygen in the atmosphere. Regarding the possible electron density decrease in the topside ionosphere, Leonovich and Taschilin [35] concluded that it can be related to changes in the 15–20 nm, 30–35 nm and 35–40 nm bands. Liu et al. [19] affirmed that the changes in the vertical plasma density gradient are mainly due to EUV 15.5–79.8 nm.

In our case during both flares, EUV radiation at 25.6 nm played the major role, which is in accord with the results of some authors mentioned above. Surprisingly, during the X1.3-flare X-ray flux, the impact was of the same level as the EUV 25.6 nm in the F2 region. During the M9.6-flare, EUV spectral bands of 28.4, 30.4 and 121.6 nm also showed strong correlation with the ionospheric F2 response. Basically, the comparison of our results with other works implies that the di decrease was a physical effect.

To sum up, a coherent di response was observed at all LoSs during the first flare and almost at all LoSs during the second flare. X1.3 flare provoked small- and medium-scale ionospheric irregularities. The M9.6-flare provoked mostly medium-scale irregularities. These disturbances can be characterized by the electron concentration change of 1–5% of the background variation (small-scale) and 5–30% of the background variation (medium-scale).

Such deviations correspond to the dI amplitudes. According to the form of the dI(10–20) curves and the results of Tables 6 and 7, it seems that the duration of the ionospheric response corresponds to dI variation filtered with the windows (10–20) min. During both flares, the response consisted of the negative dI bay observed after the onset of the flare, which was followed by the positive dI peak observed between the rapid increase of radiation at particular EUV and X-ray wavelengths and the end of the flare. During the less intense flare, the positive dI deviation was not pronounced at some LoSs. In general, the amplitudes of dI(10–20) deviations were lower than in the case of the more intense flare. To note, in both cases, the response was not intense, as other effects (e.g., multipath effect) manifested themselves in the dI variations stronger. The presence of the negative dI may be explained by the filtering procedure or have the physical meaning. There are some indirect indications in favor of the latter. However, without low-orbit satellite data, it is impossible to make a definitive conclusion on this issue.

5. Conclusions

Manifestations of two intense flares were studied in the ionosphere of the low- to mid-latitude North American sector (mostly Mexican region). The end of March 2022 was characterized by the notable change in the background solar activity represented by the F10.7-index. However, this circumstance did not have much effect on the ionospheric response to the flares on 30–31 March 2022. This is because during the flares, not only the intensification of solar radiation but also the significant change in the spectrum of solar radiation (radiation at different bands) plays an important role. Studying the impact of these processes on such regions as Mexico, combining several methods, allows us to compare the results with previous studies and obtain new data. This is especially important because of the increase in the number of solar flares expected due to the solar activity growth at the ascending part of the solar cycle 25. The peculiarity of the present study is the high temporal resolution of the ionosonde data (2 min) and the GNSS-derived data (30 s). The following results were obtained:

(1) The more intense X1.3-flare on 30 March 2022 provoked a more significant response in the lower ionosphere (including the HF fadeout event) than the less intense M9.6-flare on 31 March 2022.

(2) The narrowing of the frequency operation range and the signal amplitude decrease on ionograms manifested themselves with a ~3 min delay from the X1.3-flare onset and ~5 min delay from the M9.6-flare onset.

(3) X1.3-flare caused the shortwave fadeout near the flare peak moment (maximal radiation), which lasted ~6 min in Mexico and ~(1–8) min in Eglin. No fadeout event was caused by the M9.6-flare. For both considered flares, the maximal flare impact on the amplitude of the received signal in Mexico was observed ~(14–15) min after the flare beginning.

(4) The recovery of the lower ionosphere conditions (absorption) began before the X1.3 flare end and lasted after it, being more rapid at Eglin than in Mexico. As for M9.6 flare, the responses at two observation points were rather synchronized due to the more similar illumination conditions (LT of the flare) at two meridians than the day before, when X1.3-flare occurred.

(5) The overall X1.3-flare effects in the lower ionosphere lasted ~1 h 24 min and those of the M9.6-flare ~40 min. In both cases, the effects in the lower ionosphere lasted longer than the flare duration, in contrast to the effects revealed by GNSS data (F2 layer and topside ionosphere).

(6) The analysis of different spectral bands of solar radiation confirmed the major role of X-rays in the electron concentration increase in the lower ionosphere during the flares. At the same time, the analysis showed that the EUV impact on the lower ionosphere cannot be totally discarded. It was more pronounced for the more intense flare.

(7) For the particular cases of the two considered flares, EUV emission in the 28.4 nm spectral band provoked the weakest impact on the absorption conditions in the lower

ionosphere (probably due to the smooth gradual increase of radiation in this band) and the 133.5 nm band had the most pronounced impact.

(8) A coherent (simultaneous) dI response (implying the integral response in the F2-layer and topside ionosphere) was observed at all LoSs during the X1.3-flare and almost at all LoSs during the M9.6-flare. Both consisted of the negative dI bay after the flare onset, followed by the positive dI peak observed between the rapid increase of radiation at the particular EUV and X-ray wavelengths and the end of the flare. During the less intense flare, the positive dI were not pronounced at some LoSs.

(9) In both cases, the dI response was not as intense as the other effects (e.g., multipath effect). Notwithstanding the small amplitudes of dI deviations, the simultaneity and uniformity of the response at all LoSs, as well as the moment of the ionospheric response occurrence, leave no doubt that it was caused exactly by the flare. The ionospheric response duration corresponded to dI filtered with the centered moving average with (10–20) min windows. The dI(10–20) deviation amplitudes were smaller during the less intense flare.

(10) The preliminary conclusion is that the ionospheric response by dI depended more on the AR position on the Sun and the flare class than on the solar zenith angle. However, more statistics is needed.

(11) It was revealed that the X1.3-flare provoked small- and medium-scale ionospheric irregularities, and the M9.6-flare provoked mostly medium-scale irregularities in the F-layer.

(12) The presence of the negative dI may be explained by the filtering procedure or have the physical meaning. There are some indirect indications in favor of the last mentioned. However, in the absence of low-orbit satellite data, it was impossible to make a definitive conclusion on this issue.

(13) EUV is known to play the main role in the F2 region of the ionosphere. During the X1.3-flare, EUV radiation at 25.6 nm had the major impact on dI(10–20). Surprisingly, X-ray flux of both shorter and longer wavelengths showed a strong correlation with dI(10–20) which was of the same level as EUV at 25.6 nm. ROTI was affected by 117.5, 133.5 and 140.5 nm bands. Similar to the lower ionosphere, the 28.4 nm band impact on the F2-layer was rather low but only during the X1.3-flare. During the M9.6-flare, 25.6, 28.4, 30.4 and 121.6 nm EUV spectral bands showed strong correlation with the ionospheric response. Radiation at 25.6 nm again played a major role (very strong correlation, $r = 0.97$).

Supplementary Materials: Maps of sub-ionospheric points over Mexico for the flare periods during 30 March 2022 and 31 March 2022 are available in the Zenodo repository at <https://doi.org/10.5281/zenodo.7363050> (accessed on 27 November 2022).

Author Contributions: Conceptualization, M.A.S.; methodology, M.A.S., O.A.M. and A.M.V.; experiment design, M.A.S., A.M.V., A.G.C. and D.V.B.; experiment performance and data acquisition, E.A.-M., P.V., I.D.O.-L., V.J.G.-A., A.M.-M., M.R.-M., E.A.-R. and L.X.G.; data processing and validation, A.M.V., I.D.O.-L., A.G.C., V.J.G.-A., A.M.-M. and L.X.G.; data analysis, M.A.S., D.V.B., O.A.M. and J.A.G.-E.; visualization, M.A.S., A.M.V. and M.R.-M.; resources, J.A.G.-E.; writing—original draft preparation, M.A.S. and O.A.M.; writing—review and editing, M.A.S. and O.A.M. All authors have read and agreed to the published version of the manuscript.

Funding: LANCE acknowledges partial support from CONACyT-AEM, Grant 2017-01-292684 and CONACyT LN-315829. L.X. Gonzalez was supported by the CONACyT-AEM Grant AEM-2018-01-A3-S-63804. E. Aguilar-Rodriguez was supported by DGAPA/PAPIIT project IN103821. M. Rodriguez-Martinez was supported by the DGAPA PAPIME project PE103419 and the CONACyT grant INFR:253691. O.A. Maltseva was supported by Ministry of Science and Higher Education of the Russian Federation (State task in the field of scientific activity 2023). A. Vesnin was supported by the Ministry of Education and Science (Basic Research Program II.16). V.J. Gatica-Acevedo and A. Melgarejo-Morales express their gratitude to CONACyT.

Data Availability Statement: The OMNI data (Dst and F10.7 indices) were obtained from the GSFC/SPDF OMNIWeb interface at <https://omniweb.gsfc.nasa.gov> (accessed on 25 December 2022). The authors also thank NOAA's National Centers for Environmental Information and NOAA's Space Weather Prediction Center for the opportunity to use GOES satellite data available at <https://data.ngdc.noaa.gov/platforms/solar-space-observing-satellites/goes/> (accessed on 25 December 2022) and at www.swpc.noaa.gov/products/goes-x-ray-flux (accessed on 25 December 2022), correspondingly. The data shown in Figure 2b,c are supplied by courtesy of SolarMonitor.org. The sTEC values used to obtain dI series were derived from GNSS data from stations of (a) TLALOCNet and SSN-TLALOCNet networks, whose data is available at both TLALOCNet (<http://tlalocnet.udg.mx>, accessed on 25 December 2022) and UNAVCO (<http://unavco.org>, accessed on 25 December 2022) data archives and (b) SSN GPS network, whose data is available upon request to SSN (www.ssn.unam.mx, accessed on 25 December 2022). The authors express their gratitude to the services of DIDBase (<https://ulcar.uml.edu/DIDBase>, accessed on 25 December 2022) for the ionosonde data available for educational purposes. Other data used in this study are available in the Zenodo repository at doi:10.5281/zenodo.7363174 (accessed on 25 December 2022).

Acknowledgments: The authors also thank NOAA's National Centers for Environmental Information for the opportunity to download GOES satellite data. This work is based on GPS data provided by TLALOCNet at Servicio de Geodesia Satelital [39] and the Servicio Sismológico Nacional [40], both at the Instituto de Geofísica, Universidad Nacional Autónoma de México (UNAM) with support from UNAM-PAPIIT project IN107321, and the National Science Foundation grant 2025104 to the College of New Jersey, and also the GAGE facility operated by UNAVCO, Inc. with support from the National Science Foundation, the National Aeronautics and Space Administration, and the U.S. Geological Survey under NSF Cooperative Agreement EAR-1724794. We gratefully acknowledge the personnel from SGS, especially Luis Salazar-Tlaczani, as well as all the personnel from SGS and UNAVCO, for station maintenance, data acquisition, IT support and data distribution. GNSS station locations are indicated in Figure 3. The maps of sub-ionospheric points and animations based on these maps were constructed using the SIMuRG online tool [25]. The authors express their gratitude to this service for the opportunity of map construction and to GNSS data providers whose data are used by SIMuRG, in particular the following networks: International GNSS Service (IGS), UNAVCO, Northern California Earthquake Data Center, of Continuously Operating Reference Stations (CORS) managed by the National Geodetic Survey (NGS), an office of NOAA's National Ocean Service. We thank the anonymous reviewers for their comments and suggestions.

Conflicts of Interest: The authors declare no conflict of interest. The funders had no role in the design of the study; in the collection, analyses or interpretation of data; in the writing of the manuscript; or in the decision to publish the results.

References

1. Bryunelli, B.E.; Namgaladze, A.A. *Physics of the Ionosphere*; Nauka: Moscow, Russia, 1988; 528p, ISBN 5-02-000716-1.
2. Davies, K. *Ionospheric Radio Propagation*; Monograph 80; National Bureau of Standards: Gaithersburg, MD, USA, 1965; 487p.
3. Mitra, A.P. *Ionospheric Effect of Solar Flares*; Reidel: Norwell, MA, USA, 1974.
4. Berngard, O.I.; Ruohoniemi, J.M.; Nishitani, N.; Shepherd, S.G.; Bristow, W.A.; Miller, E.S. Attenuation of decameter wavelength sky noise during X-ray solar flares in 2013–2017 based on the observations of midlatitude HF radars. *J. Atmos. Sol.-Terr. Phys.* **2018**, *173*, 1–13. [[CrossRef](#)]
5. Mendillo, M.; Evans, J.V. Incoherent scatter observations of the ionospheric response to a large solar flare. *Radio Sci.* **1974**, *9*, 197–203. [[CrossRef](#)]
6. Blagoveschensky, D.V.; Sergeeva, M.; Raita, T. Riometer absorption during four similar storms. *Adv. Space Res.* **2022**, *69*, 1. [[CrossRef](#)]
7. Barta, V.; Sátori, G.; Berény, K.A.; Kis, A.; Williams, E. Effects of solar flares on the ionosphere as shown by the dynamics of ionograms recorded in Europe and South Africa. *Ann. Geophys.* **2019**, *37*, 747–761. [[CrossRef](#)]
8. Zaalov, N.Y.; Moskaleva, E.V.; Rogov, D.D.; Zernov, N.N. Influence of X-ray and polar cap absorptions on vertical and oblique sounding ionograms on different latitudes. *Adv. Space Res.* **2015**, *56*, 2527–2541. [[CrossRef](#)]
9. Liu, L.B.; Wan, W.X.; Chen, Y.D.; Le, H.J. Solar activity effects of the ionosphere: A brief review. *Chin. Sci. Bull.* **2011**, *56*, 1202–1211. [[CrossRef](#)]
10. Mendillo, M.; Klobuchar, J.A.; Fritz, R.B.; da Rosa, A.V.; Kersle, L.; Yeh, K.C.; Flaherty, B.J.; Rangaswamy, S.; Schmid, P.E.; Evans, J.V.; et al. Behavior of the Ionospheric F Region during the Great Solar Flare of 7 August 1972. *J. Geophys. Res.* **1974**, *79*, 4.

11. Berdermann, J.; Kriegel, M.; Banyrs, D.; Heymann, F.; Hoque, M.M.; Wilken, V.; Borries, C.; HeBelbarth, A.; Jakowski, N. Ionospheric response to the X9.3 Flare on 6 September 2017 and its implication for navigation services over Europe. *Space Weather* **2018**, *16*, 1604–1615. [[CrossRef](#)]
12. Rathore, V.S.; Kumar, S.; Singh, A.K.; Singh, A.K. Ionospheric response to an intense solar flare in equatorial and low latitude region. *Indian J. Phys.* **2018**, *92*, 1213–1222. [[CrossRef](#)]
13. Kelley, M.C. *The Earth's Ionosphere: Plasma Physics and Electrodynamics*, 2nd ed.; International Geophysics Series 96; Elsevier: Amsterdam, The Netherlands, 2009; ISBN 978-0-12-088425-4.
14. Hunsucker, R.D.; Hargreaves, J.K. *The High-Latitude Ionosphere and Its Effects on Radio Propagation*; Cambridge University Press: Cambridge, UK, 2003.
15. Dmitriev, A.V.; Yeh, H.-C.; Chao, J.-K.; Veselovsky, I.S.; Su, S.-Y.; Fu, C.C. Top-side ionosphere response to extreme solar events. *Ann. Geophys.* **2006**, *24*, 1469–1477. [[CrossRef](#)]
16. Mendillo, M.; Erickson, P.J.; Zhang, S.-R.; Mayyasi, M.; Narvaez, C.; Thiemann, E.; Chamberlain, P.; Andersson, L.; Peterson, W. Flares at Earth and Mars: An ionospheric escape mechanism? *Space Weather* **2018**, *16*, 1042–1056. [[CrossRef](#)]
17. Leonovich, L.A.; Tashchilin, A.V. Disturbances in the Topside Ionosphere during Solar Flares. *Geomagn. Aeron.* **2008**, *48*, 759–767. [[CrossRef](#)]
18. Afraimovich, E.L.; Astafyeva, E.I.; Demyanov, V.V.; Edemskiy, I.K.; Gavrilyuk, N.S.; Ishin, A.B.; Kosogorov, E.A.; Leonovich, L.A.; Lesyuta, O.S.; Palamartchouk, K.S.; et al. A review of GPS/GLONASS studies of the ionospheric response to natural and anthropogenic processes and phenomena. *J. Space Weather Space Clim.* **2013**, *3*, A27. [[CrossRef](#)]
19. Liu, X.; Liu, J.; Wang, W.; Zhang, S.-R.; Zhang, K.; Lei, J.; Liu, L.; Chen, X.; Li, S.; Zhang, Q.-H.; et al. Explaining solar flare-induced ionospheric ion upflow at Millstone Hill (42.6 N). *J. Geophys. Res.-Space* **2022**, *127*, e2021JA030185. [[CrossRef](#)]
20. Habarulema, J.B.; Tshisaphungo, M.; Katamzi-Joseph, Z.T.; Matamba, T.M.; Nndanganeni, R. Ionospheric response to the M- and X-class solar flares of 28 October 2021 over the African sector. *Space Weather* **2022**, *20*, e2022SW003104. [[CrossRef](#)]
21. Le, H.J.; Liu, L.B.; Chen, Y.D.; Zhang, H. Anomaly distribution of ionospheric total electron content responses to some solar flares. *Earth Planet. Phys.* **2019**, *3*, 481–488. [[CrossRef](#)]
22. Yasyukevich, Y.; Astafyeva, E.; Padokhin, A.; Ivanova, V.; Syrovatskii, S.; Podlesnyi, A. The 6 September 2017 X-class solar flares and their impacts on the ionosphere, GNSS, and HF radio wave propagation. *Space Weather* **2018**, *16*, 1013–1027. [[CrossRef](#)] [[PubMed](#)]
23. Reinisch, B.W.; Galkin, I.A. Global ionospheric radio observatory (GIRO). *Earth Planets Space* **2011**, *63*, 377–381. [[CrossRef](#)]
24. Maletckii, B.; Yasyukevich, Y.; Vesnin, A. Wave Signatures in Total Electron Content Variations: Filtering Problems. *Remote Sens.* **2020**, *12*, 1340. [[CrossRef](#)]
25. Yasyukevich, Y.V.; Kiselev, A.V.; Zhivetiev, I.V.; Edemskiy, I.K.; Syrovatskii, S.V.; Maletckii, B.M.; Vesnin, A.M. SIMuRG: System for Ionosphere Monitoring and Research from GNSS. *GPS Solut.* **2020**, *24*, 69. [[CrossRef](#)]
26. Pi, X.; Mannucci, A.J.; Lindqwister, U.J.; Ho, C.M. Monitoring of global ionospheric irregularities using the worldwide GPS-network. *Geophys. Res. Lett.* **1997**, *24*, 2283–2286. [[CrossRef](#)]
27. Sergeeva, M.A. Space Weather General Concepts. In Book *Space Weather Impact on GNSS Performance*; Springer: Cham, Switzerland, 2022; pp. 89–150. [[CrossRef](#)]
28. Machol, J.L.; Eparvier, F.G.; Viereck, R.A.; Woodraska, D.L.; Snow, M.; Thiemann, E.; Woods, T.N.; McClintock, W.E.; Mueller, S.; Eden, T.D.; et al. GOES-R Series Solar X-ray and Ultraviolet Irradiance. In Book *GOES-R Series*; Elsevier: Amsterdam, The Netherlands, 2020; pp. 233–242. [[CrossRef](#)]
29. Syrovatskiy, S.V.; Yasyukevich, Y.V.; Vesnin, A.M.; Edemskiy, I.K.; Voeykov, S.V.; Zhivetiev, I.V. The effect of solar flares on the ionosphere of the Earth during 24th cycle of solar activity. *Mem. Fac. Phys. Mosc. Univ.* **2018**, *4*, 1840403.
30. Kunitsyn, V.E.; Nazarenko, M.O.; Nesterov, I.A.; Padokhin, A.M. Solar Flare Forcing on Ionization of Upper Atmosphere. Comparative Study of Several Major X-Class Events of 23rd and 24th Solar Cycles, Physics of Earth, Atmosphere and Hydrosphere. *Mosc. Univ. Phys. B* **2015**, *70*, 312–318. [[CrossRef](#)]
31. Le, H.; Liu, L.; Chen, Y.; Wan, W. Statistical analysis of ionospheric responses to solar flares in the solar cycle 23. *J. Geophys. Res.-Space* **2013**, *118*, 576–582. [[CrossRef](#)]
32. Donnelly, R.F. Empirical models of solar flare X ray and EUV emission for use in studying their E and F region effects. *J. Geophys. Res.* **1976**, *81*, 4745–4753. [[CrossRef](#)]
33. Qian, L.; Burns, A.G.; Chamberlin, P.C.; Solomon, S.C. Flare location on the solar disk: Modeling the thermosphere and ionosphere response. *J. Geophys. Res.* **2010**, *115*, e2009JA015225. [[CrossRef](#)]
34. Thome, G.D.; Wagner, L.S. Electron density enhancements in the E and F regions of the ionosphere during solar flares. *J. Geophys. Res.* **1981**, *76*, 6883–6895. [[CrossRef](#)]
35. Leonovich, L.A.; Tashchilin, A.V. Aeronomic effects of the solar flares in the topside ionosphere. *Earth Planets Space* **2009**, *61*, 643–648. [[CrossRef](#)]
36. Lin, M.-Y.; Ilie, R. A Review of Observations of Molecular Ions in the Earth's Magnetosphere-Ionosphere System. *Front. Astron. Space Sci.* **2022**, *8*, 745357. [[CrossRef](#)]
37. Leonovich, L.A.; Tashchilin, A.V.; Portnyagina, O.Y. Dependence of the Ionospheric Response on the Solar Flare Parameters Based on the Theoretical Modeling and GPS Data. *Geomagn. Aeron.* **2010**, *50*, 201–210. [[CrossRef](#)]

38. Hernández-Pajares, M.; García-Rigo, A.; Juan, J.M.; Sanz, J.; Monte, E.; Aragón-Ángel, A. GNSS measurement of EUV photons flux rate during strong and mid solar flares. *Space Weather* **2012**, *10*, e2012SW000826. [[CrossRef](#)]
39. Cabral-Cano, E.; Pérez-Campos, X.; Márquez-Azúa, B.; Sergeeva, M.A.; Salazar-Tlaczan, L.; DeMets, C.; Adams, D.; Galetzka, J.; Hodgkinson, K.; Feaux, K.; et al. TLALOCNet: A Continuous GPS-Met Backbone in Mexico for Seismotectonic, and Atmospheric Research. *Seismol. Res. Lett.* **2018**, *89*, 373–381. [[CrossRef](#)]
40. Pérez-Campos, X.; Espíndola, V.H.; Pérez, J.; Estrada, J.A.; Monroy, C.C.; Bello, D.; González-López, A.; Gonzalez Avila, D.; Contreras Ruiz Esparza, M.G.; Maldonado, R.; et al. The Mexican National Seismological Service: An Overview. *Seismol. Res. Lett.* **2018**, *89*, 318–323. [[CrossRef](#)]

Disclaimer/Publisher’s Note: The statements, opinions and data contained in all publications are solely those of the individual author(s) and contributor(s) and not of MDPI and/or the editor(s). MDPI and/or the editor(s) disclaim responsibility for any injury to people or property resulting from any ideas, methods, instructions or products referred to in the content.